Estuarine hydrodynamic patterns and hydrokinetic energy production: The Douro estuary case study

I. Iglesias [a, *], A. Bio [a], L. Bastos [a, b], P. Avilez-Valente [a, c]

[a] Interdisciplinary Centre of Marine and Environmental Research (CIIMAR/CIMAR), University of Porto, Terminal de Cruzeiros Do Porto de Leixões, Av. General Norton de Matos S/n, 4450-208, Matosinhos, Portugal
[b] Department of Geosciences Environment and Spatial Planning, Faculty of Sciences of the University of Porto (FCUP), Rua Campo Alegre 687, 4169-007, Porto, Portugal
[c] Faculty of Engineering, University of Porto, Rua Dr. Roberto Frias S/n, 4200-465, Porto, Portugal

ARTICLE INFO

ABSTRACT

Influenced by both marine and river flows, estuaries can present a high potential for hydrokinetic energy exploitation. In this study, the hydrokinetic energy production in the Douro estuary was evaluated through hydrodynamic numerical modelling. The model analysed the tide and river flow, reproduced the combined effects of these two factors on the main current velocity patterns, and identified the estuarine locations with the highest potential for energy exploitation. Given the river's high variability caused by the precipitation patterns in the hydrographic basin area and the river's torrential regime, several discharge scenarios were explored, combining spring and neap tides, and high and low river flows. The results revealed that the region with the highest potential is located in the upper part of the estuary, where the highest-velocity currents were achieved for mid-ebb tide conditions and strong river flows. It was also found that tides reinforce the hydrokinetic energy production during ebb tide, although they are not strong enough to produce high values of hydrokinetic energy, being the river flow the main forcing. This work demonstrates the relevance of choosing parametrized magnitudes that are not dependent on a specific equipment, as well as the importance of a proper characterization of the estuarine hydrodynamic patterns needed to optimize the hydrokinetic energy exploitation.

1. Introduction

Estuarine regions are densely populated areas concentrating several anthropogenic activities, such as human settlements, leisure, tourism, fisheries and other marine industries. In the last decades, the population, urbanization and economic assets have experienced a rapid growth in these coastal areas, and a continuous increase of population is expected for the near future [1–3]. Associated with this increase in population, is also a rising worldwide energy demand, which has led to a rise in the use of carbon-free and renewable clean energy sources for electricity generation, to cover the increasing energy deficit [4]. So, to support human activities and marine industries, as well as to promote the protection of the environment, new sustainable and efficient sources of energy should be considered. In that sense, there has been an increasing interest in the exploitation of marine and hydro-energies, because oceans, rivers and estuaries represent a vast resource for renewable energy generation [4–8]. One of the renewable clean energy sources with high potential and reduced environmental impact is hydrokinetic energy [9–11].

Hydrokinetic energy can be extracted from river streams, tidal currents, ocean currents, man-made water canals, natural channels or waves. The technologies developed to convert the hydrokinetic energy into electricity are the marine current energy conversion (MCEC) systems. MCEC systems, which present some potential for this study, can further be classified as tidal in-stream energy converters (TISEC), marine current turbines (MCT) and river energy conversion systems (RCECS) [12,13].

This kind of energy production presents several advantages: the predictability of the flows and, consequently, of the power production [14]; a high load factor derived from the fluid properties [15]; the possibility to extract energy with minimum environmental impact and no land occupation [16]; and, the fact that these

* Corresponding author.
E-mail addresses: iiglesias@ciimar.up.pt, isabel.iglesias.fdz@gmail.com (I. Iglesias), anabio@ciimar.up.pt (A. Bio), lcbastos@fc.up.pt (L. Bastos), pvalente@fe.up.pt (P. Avilez-Valente).

systems are water-life friendly, with minimal visual impact, no emissions and no noise [7,14]. The advantages of this energy source are even more evident when estuarine regions are considered for the installation of energy extraction devices adapted for depth-limited regions. Estuaries can achieve significant power levels in regions with relatively modest tidal range [16]. They are generally located nearby power consumption points, such as cities, industries or ports; this closeness allows the reduction of operational costs when compared with offshore farms as well as facilitates the installation and maintenance of the equipment. Furthermore, estuaries are relatively protected environments, both in terms of meteorology and ocean impacts, where extreme flow velocities that could damage the equipment are generally infrequent [17,18]. However, the installation and the operation of MCEC systems can have harmful effects on the estuarine natural environments, associated with changes in circulation patterns and sediment transport due to turbulent mixing and a reduction in velocity across the rotor plane [4,9,13,19–22]. These effects should be analysed previously to the installation of hydrokinetic energy extraction equipment.

Hydrokinetic energy can be obtained from different phenomena, such as tidal and oceanic currents, baroclinic circulation or barotropic flows from river discharges. In regions where several of these driving agents occur, like estuaries, the hydrokinetic resource exploitation should be analysed considering their combined effects [23]. Estuarine hydrology can be complex, with ebb-flood asymmetry and complex geomorphologies that can limit the maximum extractable power [16]. Therefore, to analyse the hydrokinetic production capacity of estuarine regions, hydrodynamic numerical models have emerged as key tools, becoming increasingly relevant as decision-making and support tools for an effective and integrated marine and coastal management [24]. Numerical solutions provide a deep understanding of the physical properties of complex estuarine environments, properly depicting the estuarine hydrodynamic patterns [25], and a considerable effort has been made to provide the most accurate numerical estimations for the complex estuarine circulation [1].

In that sense, validated hydrodynamic numerical models, based on real bathymetry, tide and river flow data, are essential tools to quantify energy resources and to define the areas with the greatest potential for the emplacement of new hydrokinetic energy farms,

forecasting, with high confidence, flow dynamics and energy production [14,26]. This is especially important in estuarine regions, where the complex geometry of the basin (shallow waters combined with narrow sections) and limitations due to water depth and estuarine traffic can impose strong restrictions to turbine installation and operation, even when considering the third generation of Hydrokinetic Energy Converters (HECs), which are compact systems designed to operate in shallow water regions with relatively low current velocities and reduced environmental impact [17,18,23].

In this work, the hydrokinetic resource exploitation in the Douro estuary was evaluated with the help of numerical modelling tools. The implemented model and model scenarios were chosen aiming to reproduce the variability of the combined effects of tide and river flow on the main current velocity patterns, as well as to identify the estuarine locations with the highest potential for energy exploitation. Additionally, the relevance of choosing parametrized magnitudes that are not dependent on a specific equipment for hydrokinetic resource characterization was demonstrated.

2. Study region

The Douro is the river with the largest basin of the Iberian Peninsula. It flows into the Atlantic Ocean in an urban estuary surrounded by two large cities, Porto and Vila Nova de Gaia (northwest Iberian coast, cf. Fig. 1). It is a highly dynamic, funnel-shaped, mesotidal and narrow estuary, with a high interannual river flow variability. The river has the standard normal flow pattern for its latitude, associated with the annual precipitation cycle [27], featuring strong estuarine flows in winter and weaker flows in summer. Its torrential regime produces recurrent severe floods and strong currents that cause serious damage to the riverine populations and problems to the fluvial navigation [28,29]. About 21 km upriver, the estuary is limited by the Crestuma-Lever dam, used for hydroelectric production, where the freshwater discharge can reach values over 13 000 m^3/s [30]. Due to the power plant operating regime, the freshwater discharge usually presents a cyclic pulse pattern, having a strong effect on the flow velocity and on the estuarine circulation. Along with the strong effect of freshwater flows, tides are the next major hydrodynamic forcing in this
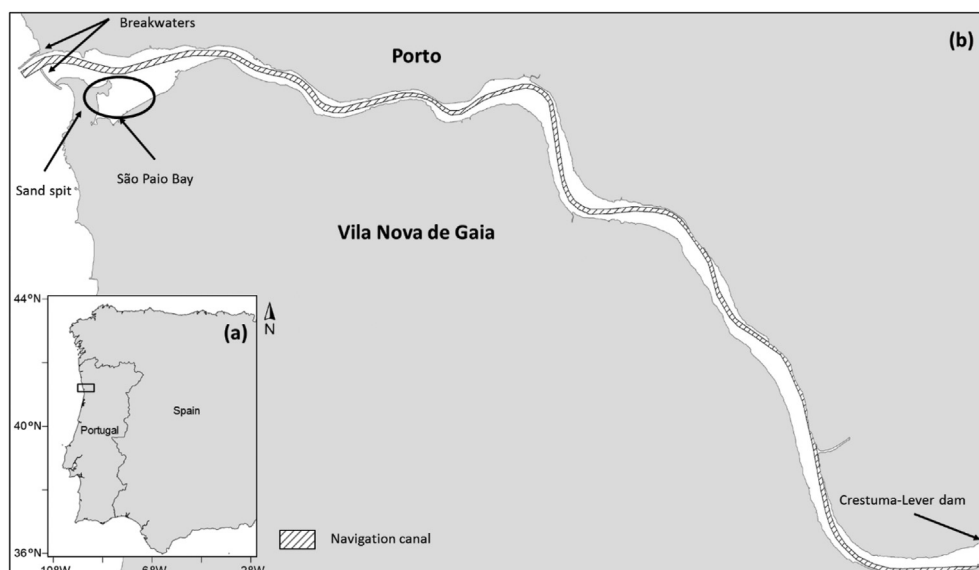

Fig. 1. Douro estuary configuration.

estuary. Local tides have a semi-diurnal regime with a 12.4 h-long period. M2 is the main constituent, followed by S2, N2 and K2. The semi-diurnal frequency band dominates the tidal signal throughout the estuary with a tidal forcing factor with a value of 0.09 [31,32]. Inside the estuary, tides are slightly progressive, with time delays of 12−17 min from the mouth to the upstream end of the estuary and a slight amplification between 2 and 4% [31]. During river floods, the freshwater masses are thoroughly flushed to the sea, inducing quite strong currents that can reach velocities up to 8 m/s, and preventing seawater intrusion, even in spring tide conditions. For low river discharges, tidal currents become dominant, and the ocean water enters the estuarine region with a salt-wedge configuration [33].

Circulation patterns in this estuary are also conditioned by its irregular bathymetry and by the configuration of its margins (see Fig. 2). Depths are generally between 0 and 10 m. Although, depths up to 28 m can be found at narrower sections, outer bends, and sediment extraction sites [29]. The estuary presents a sandspit, made up of maritime and fluvial sediments, that partially obstructs the entry of ocean water, acting as a natural barrier against storm waves and protecting the estuarine margins and harbours.

Anthropogenic interventions in the estuarine region have changed the estuarine hydrodynamics and erosion/accretion patterns [34]. To stabilize the formerly dynamic inlet sandspit, the northern breakwater of the estuary inlet was extended and a seaward facing detached breakwater was built (cf. Fig. 1). Bastos et al. [28] found that these structures interfered with local sedimentary and hydrodynamic patterns, considerably increasing the area and volume of the sandspit and silting up the contiguous wetland (São Paio Bay). The sandspit that used to be breached and sometimes almost destroyed during river floods, seems now virtually unbreakable during flood episodes, and harsher flood effects can be expected, in terms of economic losses and structural damage [35]. However, this structure funnelled the estuary mouth, and the stronger currents found there increased the potential for hydrokinetic energy production.

Local clean and sustainable energy production is particularly relevant due to the high population density and energy demand. For the last years, the Porto district suffered a huge increase in tourism (from 199.2 to 874.2 guests in tourist accommodation per 100 inhabitants between 2001 and 2017), accompanied by a growth in the birth rate (from 8.2 to 9.2 births per 1000 inhabitants between 2009 and 2018). This led to a rise in electric energy consumption (from 2445.3 to 5576.9 kW·h/inhabitant per year between 2001 and 2017) [36], fostering the interest in new environment-friendly, sustainable and efficient sources, taking advantage of the tide and current conditions of this highly dynamic estuarine region.

3. Materials and methods

3.1. Numerical model

The implemented model is the 2DH version of the openTELEMAC-MASCARET, able to accurately represent estuarine hydrodynamic patterns [24,35]. It solves the depth-averaged free surface flow equations, taking into consideration several physical processes, such as bed friction, turbulence, supercritical and subcritical flows, and density effects related to horizontal temperature and salinity gradients, making it suitable for this study. The depth-averaged equations for mass and momentum conservation are:

$$\frac{\partial H}{\partial t} + \frac{\partial (Hu)}{\partial x} + \frac{\partial (Hv)}{\partial y} = 0 \tag{1}$$

$$\frac{\partial u}{\partial t} + u\frac{\partial u}{\partial x} + v\frac{\partial u}{\partial y} + fv = -g\frac{\partial \eta}{\partial y} + \frac{1}{h}\nabla \cdot (H\,\nu_T\,\nabla u) - \frac{C_f}{2h}\|\boldsymbol{u}\|u \\ -\frac{gH}{2\rho_0}\frac{\partial \rho'}{\partial y} \tag{2}$$

$$\frac{\partial v}{\partial t} + u\frac{\partial v}{\partial x} + v\frac{\partial v}{\partial y} + fu = -g\frac{\partial \eta}{\partial y} + \frac{1}{h}\nabla \cdot (H\,\nu_T\nabla v) - \frac{C_f}{2h}\|\boldsymbol{u}\|v - \frac{gH}{2\rho_0}\frac{\partial \rho'}{\partial y} \tag{3}$$

where η is the free surface elevation above the mean sea level (MSL), $H = d + \eta$ is the total water depth (d is the depth below the
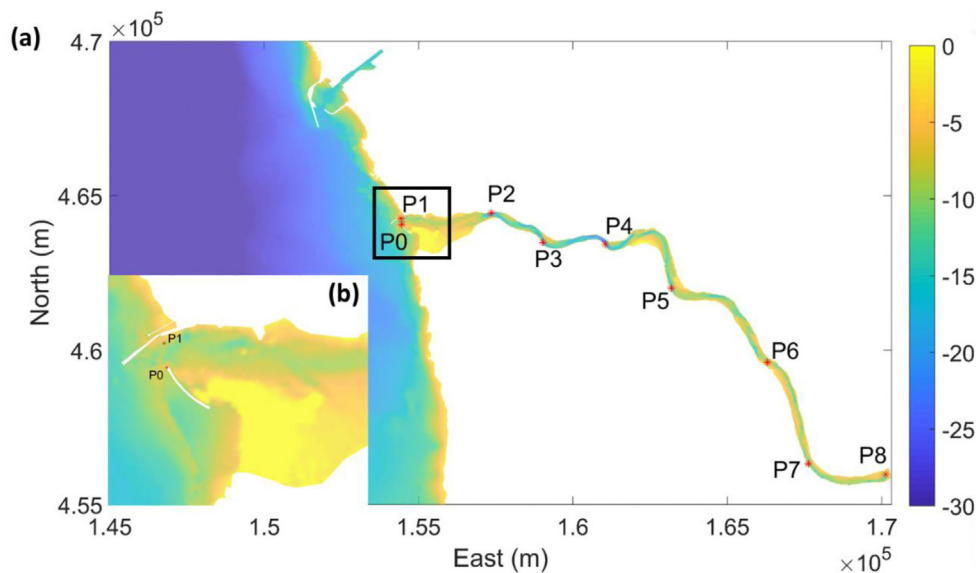

Fig. 2. (a) Computational domain (horizontal coordinates referred to Datum PT-TM06-ETRS89) and bathymetry (in metres referred to the Hydrographic Zero). The numerical water elevation/current velocity stations are shown as red asterisks. (b) Detail of the estuarine mouth. (For interpretation of the references to colour in this figure legend, the reader is referred to the Web version of this article.)

MSL), $\boldsymbol{u} = (u, v)$ is the vertically averaged velocity vector and u and v are its components in the x- and y-directions, respectively, f is the Coriolis parameter, g is the acceleration due to gravity, ν_T is the eddy viscosity, C_f is the dimensionless bottom friction coefficient, ρ_0 and ρ' are the reference and anomaly densities, such that $\rho = \rho_0 + \rho'$ is the local pressure and h is the local depth referred to the hydrographic zero (HZ) which is defined as the level of the lowest astronomical tide. The Portuguese HZ is 2 m below the MSL, so $h = d - 2$ m [37]. Mass source terms and forcing terms due to atmospheric pressure and wind friction were not considered herein but are included in Telemac2D.

To compute the local pressure, an equation of state is necessary, along with two conservation equations for the transport of two tracers: salinity and temperature (for details, see Ref. [38]).

The Telemac2D module was used with a finite element method solver for numerical discretization and integration, where the continuity equation (1) is replaced by a wave equation [39]. Telemac2D uses unstructured linear triangular meshes, which allow a good resolution of the computational domain even for complex geometries, with an improved hydrodynamic detail while at a reduced computational cost.

3.2. Model set-up

A 2DH finite element mesh was generated which covers the estuarine region from the Crestuma-Lever dam to the mouth of the estuary, and the adjacent coastal area, including the Leixões harbour, close to the northern boundary, to allow proper numerical development of the tide and of the river flow (cf. Fig. 2). Several databases were considered for the mesh construction. Bathymetry and coastline were extracted from a 2009 bathymetric survey provided by the Hydrographic Institute of the Portuguese Navy (IH) and the sandspit elevation data was taken from a 2015 topographical survey [28]. Finally, the adjacent costal bathymetry was obtained from the Bathymetric Model of Douro, provided also by the IH, and from the GEBCO database [40]. To improve the transition between land and ocean/river areas, topographic data from Portuguese military maps was used, and the different datasets were interpolated using a kriging algorithm [41,42]. The computational mesh had 60 757 triangular elements and 31 325 nodes, and its resolution varied from 300 m at the ocean boundary to 35 m at the São Paio Bay. The sandspit was considered as a wet/dry zone and the estuarine mouth breakwaters were included in the model domain as solid walls. For details on the computational mesh and modelling simulation procedures, as well as the results of the validation simulations, refer to Iglesias et al. [35]. An eddy viscosity of 1 m²/s and a Strickler friction coefficient $K_s = 30$ m$^{1/3}$/s and a time step of 6 s were adopted. The relation between the dimensionless friction coefficient and the Strickler coefficient is given by:

$$C_f = \frac{1}{K_s{}^2} \frac{2g}{H^{1/3}} \tag{4}$$

A set of five cases were run, which are supposed to model an entire year-long hydrological cycle. These correspond to five river flow scenarios, associated with key percentiles of non-exceedance. The percentiles were calculated using hourly Douro river flow data provided by Energias de Portugal (EDP) at the Crestuma-Lever dam between 1998 and 2017 (see Table 1). The river discharge was forced at the fluvial boundary with a constant value for each scenario. At the oceanic boundary, the numerical model was forced with a tide-level time series (cf. Fig. 3). Every scenario was run for a computational time length of 21 days, encompassing a complete spring-neap tidal cycle of 15.4 days, considered for the computation of the different parameters, plus an initial period of 5.6 days to allow the initial stabilization of the numerical model after a cold start with a smoothing ramp of 9 h. The time series for the tide elevation was obtained using the TPXO.2 tidal model for an offshore location within the model boundary [43], and does not include the equinox nor the solstice periods. The temperature and salinity values for the open boundaries were extracted from available in-situ data and from previously published works and set to 35.8 PSU and 17 °C for the oceanic boundary and 0 PSU and 8 °C for the river boundary [44−46].

3.3. Energy resource

The power density, p_{KE}, i.e. the flow of the water kinetic energy per unit time passing through a vertical unit area cross-section perpendicular to the flow direction, is given by:

$$p_{KE} = \frac{1}{2} \rho \, \alpha \, U^3 \tag{5}$$

where ρ is the water density, U is the flow velocity and α, which is usually set to 1, is the energy coefficient to accommodate for the velocity variation along the water column [23,47].

However, not all of this power can be converted into electricity. Water current turbines extract energy from the fluid by reducing flow velocity, so there is a theoretical limit to the percentage of kinetic energy that can be converted into harnessed energy when open free-flow turbines are considered. This limit, known as the Betz limit, is 59.3% for a single device [7]. To take into account the fluid dynamic efficiency of the turbine, the power coefficient C_p is introduced, to represent the ratio between the harnessed and the available mechanical power. The effective power density, p_E, is then [14]:

$$p_E = C_p \, p_{KE} \tag{6}$$

In practice, the actual performance of a turbine is less than the Betz limit, and a value of $C_p = 0.40$ was considered in this study [5,48]. Other types of turbines can present higher C_p values increasing the efficiency of the equipment. Venturi duct type turbines can exhibit power coefficients close to 0.85 [49]. However, this technology is still being developed and only small diameter turbines have been tested.

Then, the available energy resource of a turbine, E_e, over a time interval, T, can be obtained by integrating the effective power

Table 1
Modelling scenarios.

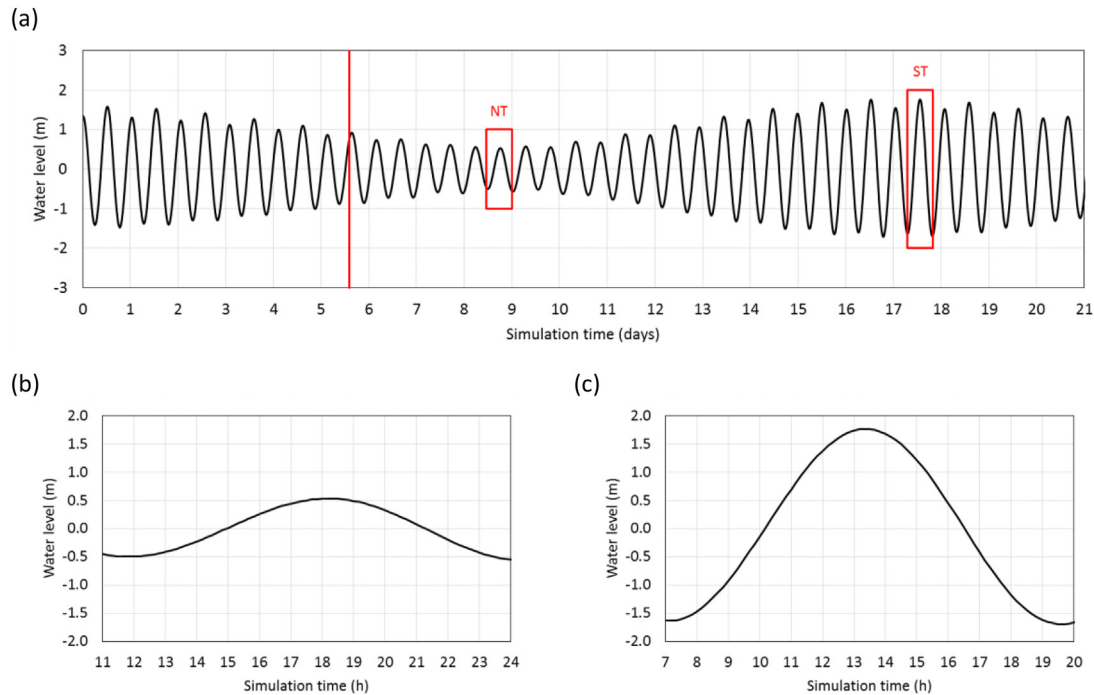| Scenario	River flow	Percentile of non-exceedance	Frequency of occurrence	Simulation length	Tide
	(m³/s)	(%)	(%)	(days)	
S1	1566	95	7.5	21	TPXO.2
S2	1214	90	7.5		
S3	801	80	20.0		
S4	298	50	25.0		
S5	0	30	40.0		

(a)

(b)

(c)

Fig. 3. (a) Open boundary tidal surface elevation, above MSL, for all modelling scenarios, from Day 1 to Day 21, (b) detail of the neap-spring tidal cycle (NT, Day 9), and (c) detail of the spring-tide tidal cycle (ST, Day 18).

density over the swept area, A, of the turbine and over the time interval [50]:

$$E_e = \int_0^T A \, p_E dt \tag{7}$$

However, each energy conversion device works within a specific range of velocities between a lower velocity threshold, the cut-in velocity, U_i, and an upper velocity threshold, the cut-off velocity, U_o [50]. Most energy conversion devices available on the market exhibit cut-in velocities around 1 m/s or above [12]. However, a few energy conversion systems present lower cut-in velocities (e.g. Ref. [51]). Devices with a lower cut-in velocity, around 0.7 m/s, are more appropriate for the Douro estuary given its hydrodynamic characteristics, and this is the value that is going to be considered in this study. The cut-off velocity is meant to decrease the risk of a device failure. Usually, cut-off velocities are in the order of 3.5 m/s [52]. In the Douro estuary, current velocities of this magnitude are achieved for winter conditions, for flow rates above 1300 m³/s [33]; velocities up to 8 m/s can be reached for extreme floods [35]. However, such events are rare, for instance a flow rate of 17 000 m³/s has a return period of 1000 years [1]. The most frequent Douro river flow rates vary between 100 m³/s and 1000 m³/s for the dry and wet seasons, respectively.

3.4. Power parametrization

Energy production depends on the choice of the turbine and on the choice of the device location. The available kinetic power is given by the product of the power density by the swept area of the turbine:

$$P_{KE} = p_{KE} \, A \tag{8}$$

Usually, a location is selected based on an analysis of the power

density, p_{KE}, and/or of the available kinetic power, P_{KE}. To make this study independent of a chosen turbine, let us define a new parameter, the maximum available kinetic power, as:

$$P_{KM} = p_{KE} \, h^2 \tag{9}$$

Such a parameter is site dependent and should be a better indicator of the available energy potential. The selection of such parametrized magnitudes that are not dependent on specific equipment are more adequate to evaluate the potential for hydro-kinetic resource production. In this study we parametrized using the local depth, h, which turns the results dependent on the estuarine location. However, this makes that high values of maximum available kinetic power and maximum available energy resource can be produced in deeper regions despite low current velocities. In this sense the obtained results should be carefully analysed.

Besides that, for each location, a parametric maximum available energy resource, over a time interval T, can be computed as:

$$E_{KM} = \int_0^T P_{KM,U} dt \quad where \quad \begin{cases} P_{KM,U} = P_{KM} \,, \; U \geq U_i \\ P_{KM,U} = 0 \,, \; U < U_i \end{cases} \tag{10}$$

Finally, the extracted energy over a period T, E_e, can be computed as

$$E_e = \frac{\pi}{4} \left(\frac{D}{h} \right)^2 \eta_{t-g} \, C_p \, E_{KM} \tag{11}$$

where D is the turbine inlet diameter, and η is the transmission−generator efficiency. In this way, the extracted energy is directly proportional to the maximum available energy resource and the ratio between D and h, which usually presents a maximum value of 0.85, is device-dependent and quite easy to quantify once a machine is chosen.

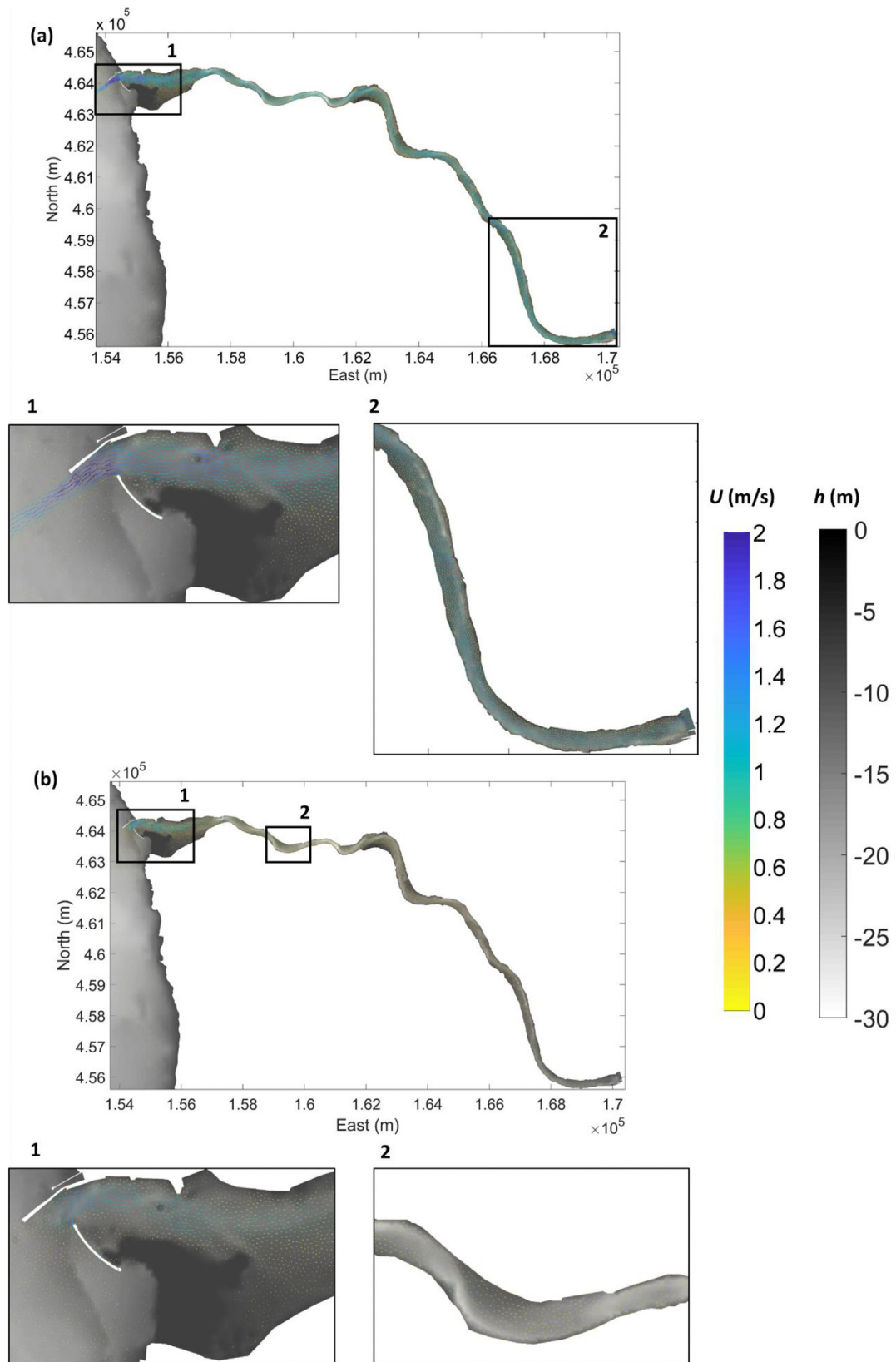To compute the kinetic power density and the maximum

Fig. 4. Maps of the estuarine depth, *h*, referred to the HZ, and of the current velocity, *U*, maps, extracted at the (a) mid-ebb of the highest spring tide for scenario S1, and (b) mid-flood of the highest spring tide for scenario S5.

Table 2

Characteristics of the numerical water elevation/current velocity gauges. Horizontal coordinates (X, Y) refer to Datum PT-TM06-ETRS89. Depths (h) refer to the HZ.

	P1	P2	P3	P4	P5	P6	P7	P8
X (m)	154 435	157 357	159 036	161 048	163 187	166 302	167 629	170 133
Y (m)	464 259	464 441	463 485	463 424	462 003	459 610	456 323	455 978
h (m)	4.83	20.42	17.41	19.18	6.77	8.95	6.43	7.39

available kinetic power associated with each scenario in Table 1, the velocity fields for each run (S1 to S5) were extracted at two instants during the tide-cycle: mid-flood and mid-ebb for a spring-tide tidal cycle (ST) (cf. Fig. 3). At these instants, the tidal velocities are at their maximum magnitude [14,50]. The energy coefficient, α, was set to 1. As the model was not calibrated for the temperature and salinity transport distributions, a pragmatic approach was taken for computation of the kinetic power density, using the equation of state of Millero et al. [53] to estimate the mass density at the numerical gauges P1−P8.

For river flows above 700 m³/s, the entire estuary region is flooded with fresh water [30]. Such discharges are more frequent during winter when the mean river water temperature is approximately 12 °C within the estuary. Therefore, for scenarios S1, S2 and S3, a density of 999 kg/m³ was assumed. For river flows below 700 m³/s, the estuary is mostly filled by seawater. Such discharges occur during summer when the water temperature in the estuary region is about 18 °C. Thus, for simulations S4 and S5, a density of 1025 kg/m³ was assumed.

Maps of the maximum available kinetic power (see Fig. 4) were analysed taking into consideration the location of the navigation canal (cf. Fig. 1). This canal has a mean depth between 6 and 8 m, with some deeper regions that usually do not exceed a 12 m depth. Due to this low depth, to the restrictions imposed by the local authorities, and to the frequent dredging operations, the installation of a device for energy production inside the canal is not possible. Therefore, a mask was applied to limit the analysis to the area outside the navigation canal. Nine stations, P0 to P8, were selected for analysis (Fig. 2 and Table 2).

4. Results and discussion

4.1. Velocity and maximum parametric power distribution

The analysis of the velocity, power density and maximum available power fields (Figs. 4−6) seem to indicate the existence of conditions for kinetic energy harvesting all over the estuary. These conditions are presented during ebb and flood conditions, with high river flow discharge for the upstream region or during both, high and low river flow discharge, in the estuarine mouth (cf. Table 3). For the scenarios with strong river flows (S1 and S2), potential optimal conditions for device installation exist in the estuarine mouth at point P1. The highest-velocity currents (~2.5 m/s) and the highest power density (~3.5 kW/m²) for the entire simulation were found at that location (see Figs. 4a and 5a).

The largest values of the maximum available power were found in the narrowing upstream the estuarine mouth (station P2, ~230 kW), around stations P3 (~230 kW) and P4 (~300 kW), and downstream of the Crestuma-Lever dam between stations P6 and P8 (~100 kW) (Fig. 6a). These maxima, are not associated either with high current velocity or with high power density values, are related with the bathymetric conditions at those locations, which present larger depths (see Fig. 2 and Table 2). On the other hand, for low river flow scenarios (S4 and S5), the potentially optimal region for device installation seems to be located at the estuary mouth. Other regions with potential for energy extraction were identified

between the mouth and the P4 station (see Fig. 4d), corresponding to the deepest zones of the entire estuary (see Fig. 2 and Table 3). However, and despite the high available power values obtained (~30 kW), current velocities in these regions are below 0.7 m/s, not reaching the cut-in velocity value assumed in this study (cf. Fig. 4b), and, therefore, no energy can be extracted. So, the estuarine zone that presents some potential for energy extraction for low river flow scenarios is the estuarine mouth, at stations P0 and P1. There, strong velocity currents of around 1.4 m/s for mid-flood conditions of a spring tide can be found, due to the narrow estuarine cross-section and to the sandspit-breakwater configuration which increase the flow velocity (cf. Fig. 4b).

Thus, when the tide state and the cut-in velocity of 0.7 m/s are considered (cf. Table 3), only two regions seem suitable for the installation of energy production devices: one at the estuarine mouth and another close to station P8. Stations P0, P1 and P8 in Fig. 2 were thus selected to represent their potential for energy extraction of the parametric power and the maximum available energy resource. The time evolution of the available power for the five river flow scenarios at the selected points is illustrated in Fig. 7.

At station P8, the time evolution pattern is very similar for the three scenarios S1, S2 and S3 (cf. Fig. 7a), when high available kinetic power values are registered close to the Crestuma-Lever dam. However, the power magnitude is different for each scenario. These differences are associated with the river flow conditions, with a higher power magnitude for a higher river discharge in scenario S1. The tide affects the maximum available power amplitude, even for locations near the upstream limit of the estuary and for a river flow larger than 1500 m³/s. Maximum values of this parameter are obtained for scenario S1 during spring tide conditions. Scenario S2 presents lower power density values than scenario S1. It must be noticed that, during the slack tides of high spring tides, the power density presents very low values associated with low current velocities. For scenario S3 low available power values are more frequent than for scenario S2.

As expected, the results for scenarios S4 and S5, at station P0, located at the estuary mouth between the breakwaters (cf. Fig. 2), show a strong dependence on the tide (see Fig. 7b). Scenario S5 presents higher values than S4, revealing that the main forcing for energy production at this location is the tide because a decrease of the production was observed with an increase of the river flow. During and close slack tides time instant, as well as during neap tides, the available power presents low values associated with low current velocity conditions for both scenarios. Notice that maximum values were obtained during mid-flood time instants, however, and that, contrary to what was expected, the available power is very small during mid-ebb time instants. This can be explained by the fact station P0 is located close to the northwestern berm of the detached breakwater, which partially masks the tide effects during ebb conditions. Available power and maximum available energy resource were also calculated at station P1, located at the estuarine mouth as well (cf. Fig. 2), and with some potential for energy extraction (Figs. 5 and 6). This point is located at the northern side of the navigation canal close to the northern breakwater of the estuary inlet. Results (cf. Fig. 7c) revealed that for scenario S4 the effect of the river flow increases the current velocity
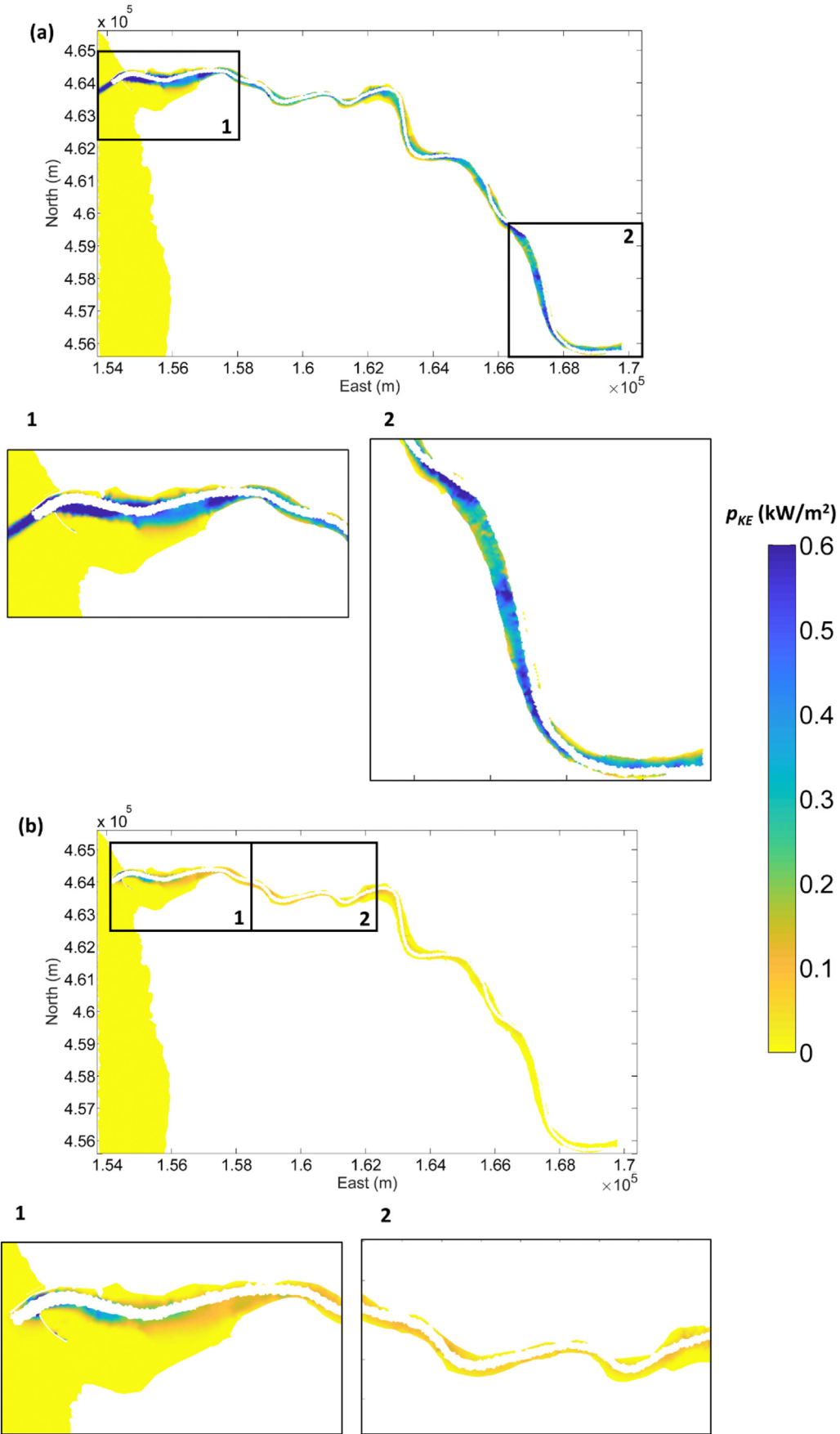
Fig. 5. Power density, p_{KE}, maps extracted at the (a) mid-ebb of the highest spring tide for scenario S1, and (b) mid-flood of the highest spring tide for scenario S5. The maps are masked with the navigation canal.

8

Fig. 6. Parametric maximum power, P_{KM}, maps extracted at the (a) mid-ebb of the highest spring tide for scenario S1, and (b) mid-flood of the highest spring tide for scenario S5. The maps are masked with the navigation canal.
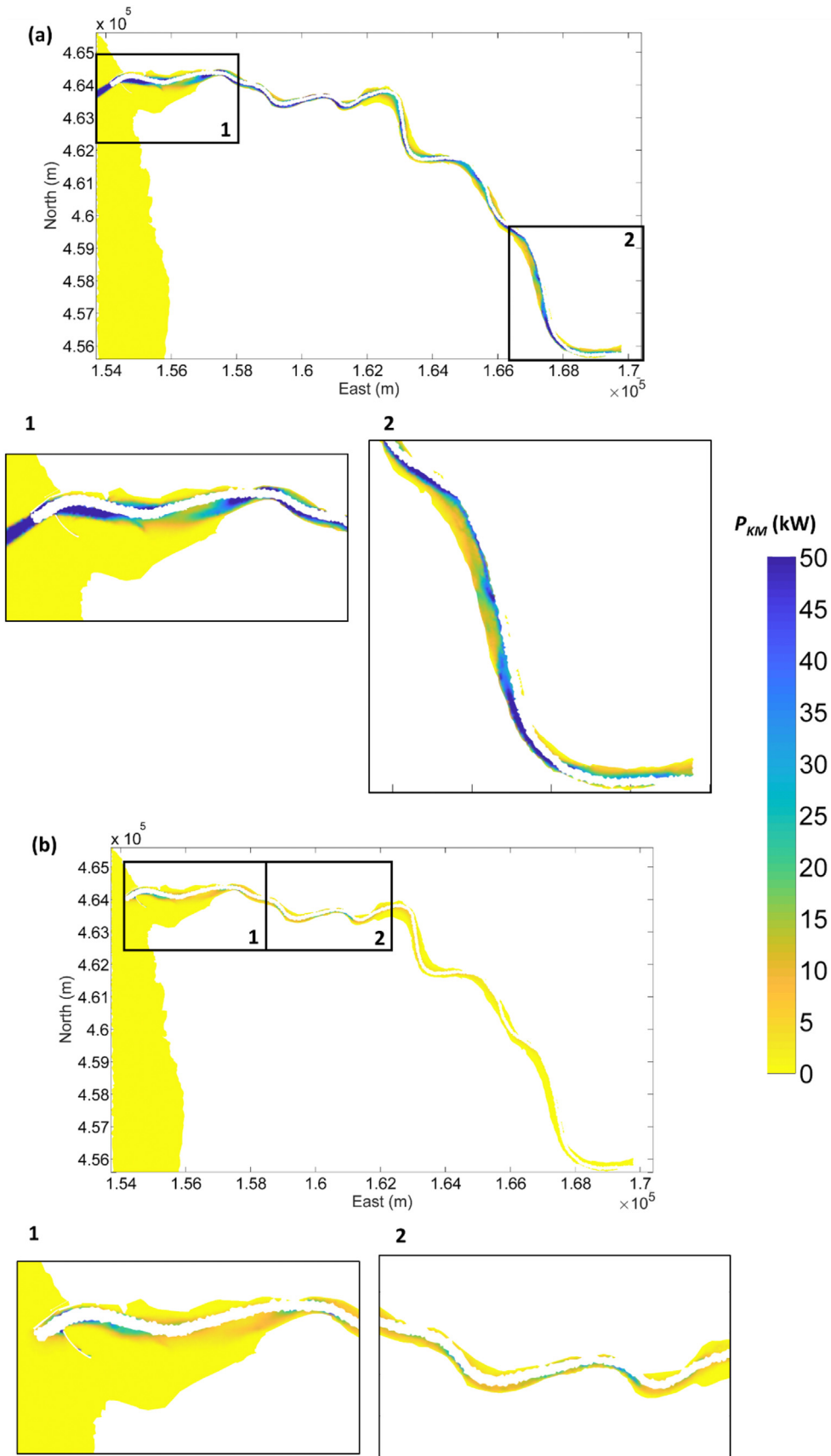
Table 3
Instantaneous maximum power, P_{KM}, at mid-flood and mid-ebb of the spring-tide (ST) with and without cut-in velocity.

			P_{KM} (kW)				
			S1-p95	S2-p90	S3-p80	S4-p50	S5-p30
P0	Mid-flood	No cut-in	0.02	0.01	1.45	10.35	17.75
		Cut-in	0.00	0.00	0.00	10.35	17.75
	Mid-ebb	No cut-in	5.89	3.19	1.36	0.77	0.59
		Cut-in	5.89	0.00	0.00	0.00	0.00
P1	Mid-flood	No cut-in	0.41	0.00	1.29	8.49	13.16
		Cut-in	0.00	0.00	0.00	8.49	13.16
	Mid-ebb	No cut-in	27.70	20.40	13.46	7.33	4.87
		Cut-in	27.70	20.40	13.46	7.33	4.87
P2	Mid-flood	No cut-in	2.19	0.16	0.05	0.61	1.19
		Cut-in	0.00	0.00	0.00	0.00	0.00
	Mid-ebb	No cut-in	24.90	17.19	10.34	4.81	2.77
		Cut-in	0.00	0.00	0.00	0.00	0.00
P3	Mid-flood	No cut-in	12.56	1.58	0.06	2.20	4.86
		Cut-in	0.00	0.00	0.00	0.00	0.00
	Mid-ebb	No cut-in	78.10	54.18	32.61	14.55	7.91
		Cut-in	78.10	54.18	0.00	0.00	0.00
P4	Mid-flood	No cut-in	6.68	0.85	0.00	0.79	2.10
		Cut-in	0.00	0.00	0.00	0.00	0.00
	Mid-ebb	No cut-in	42.38	27.70	15.15	5.94	2.89
		Cut-in	0.00	0.00	0.00	0.00	0.00
P5	Mid-flood	No cut-in	3.02	0.57	0.00	0.04	0.21
		Cut-in	0.00	0.00	0.00	0.00	0.00
	Mid-ebb	No cut-in	7.02	4.64	2.47	0.81	0.31
		Cut-in	0.00	0.00	0.00	0.00	0.00
P6	Mid-flood	No cut-in	25.26	10.86	0.98	0.01	0.74
		Cut-in	25.26	0.00	0.00	0.00	0.00
	Mid-ebb	No cut-in	28.33	16.82	7.56	1.57	0.30
		Cut-in	28.33	16.82	0.00	0.00	0.00
P7	Mid-flood	No cut-in	15.62	8.34	1.91	0.02	0.03
		Cut-in	15.62	8.34	0.00	0.00	0.00
	Mid-ebb	No cut-in	12.95	7.50	2.98	0.36	0.01
		Cut-in	12.95	7.50	0.00	0.00	0.00
P8	Mid-flood	No cut-in	60.57	50.08	26.68	0.61	0.00
		Cut-in	60.57	50.08	26.68	0.00	0.00
	Mid-ebb	No cut-in	24.04	18.13	7.98	0.52	0.00
		Cut-in	24.04	18.13	0.00	0.00	0.00

during ebb tide, and, contrary to scenario S5 which achieves the highest available power during mid-flood conditions, in scenario S4 the highest available power is achieved during mid-ebb conditions.

4.2. Hydrodynamic patterns influence on energy production

The previous section demonstrates the importance of properly selecting the estuarine locations for hydrokinetic energy extraction, based on the estuarine hydrodynamic configuration. However, it must be kept in mind that the maximum current velocity values do not necessarily occur during mid-flood and mid-ebb time instants. When the dam is discharging fresh water into the estuary, one expects the maximum current velocity to occur during ebb conditions, when tide and river align their flow directions. However, this effect depends directly on the river flow strength, on the tides and on the relation between these two drivers, and thus the hydrodynamic patterns of the estuary region under study should be carefully identified. To achieve this objective, an analysis considering the entire tidal cycle was applied to stations P1 to P8, covering the full extension of the estuary.

Water elevations recorded for stations P1 to P8 show a small delay in the propagation of the tide along the estuary for all of the simulated scenarios (cf. Fig. 8 and Table 4). For a null river discharge (scenario S5), the high tide lag is about 10 min and the tides suffer a slight amplification between 1% and 4%, in agreement with the results of Pinto and da Silva [31]. However, during the low tide of a spring tide, a higher delay of about 110 min was found. This delay,

associated with an asymmetry of the tidal curve, could be produced by bathymetric constraints and also by the non-linearity caused by energy dissipation associated with friction [24]. This asymmetry, although registered for all simulated scenarios/river discharges (cf. Fig. 8), induces a larger tidal lag in low tide conditions (cf. Table 4) and is more noticeable for stronger river discharges.

The river flow rates imposed in scenarios S1, S2, S3 and S4 are not strong enough to prevent the tide from entering the estuarine region, and the tidal pattern is visible in the recorded water elevation in all stations (cf. Fig. 8). However, these river flow rates are strong enough to produce a decrease in the tidal amplitude within the estuarine region, most noticeable in the upriver stations (P7 and P8).

When the current velocity patterns were analysed, in the absence of river flow (scenario S5, Fig. 9e), higher velocities were observed at the most downstream station (P1), decreasing upriver. The highest current velocity for this scenario was 1.11 m/s, with maxima obtained at mid-flood and secondary maxima at mid-ebb. When the river flow is considered, the maximum values obtained at mid-flood diminished because the river flow partially blocks the entrance of the tide. Then the maximum current velocities are obtained at mid-ebb when the effect of the river flow increases the current velocity (cf. Fig. 9a–d). The maximum velocity value, 1.49 m/s, was recorded for scenario S1 at station P1, close to the estuarine mouth. However, for the same scenario, large velocities were also obtained for station P8 (1.32 m/s), due to the strong river discharge. When the river flow is strong enough to increase the velocity at P8 (scenarios S1, S2, and S3, see Fig. 9a–c), the current velocity at this station only displays a small variation associated with the tide.

4.3. Energy production

The analysis of water elevation and current velocity patterns demonstrated a strong variability in the hydrodynamic behaviour of the Douro estuarine region that could affect the hydrokinetic energy production and thus the available energy resource. This available energy resource is dependent on the local depth, which will define the optimal turbine swept area for each specific location, and also the cut-in and cut-off velocities, which will constrain the operation of the installed device.

When the available energy resource is calculated for a full neap-spring tidal cycle (cf. Table 5), stations P2, P4 and P5, which displayed some potential for hydrokinetic energy extraction, revealed to have a very low to zero available energy resource. Besides that, stations P3, P6, P7 and P8, were only relevant for scenarios S1 and S2, with station P8 also presenting some potential for scenario S3. On the other hand, at station P1, the hydrokinetic energy could be successfully extracted during all of the performed scenarios, though with lower values. The annual available energy production at each station (see Table 6) can be estimated by taking into consideration the frequency of occurrence associated with each scenario (cf. Table 1). Thus:

$$E_{KM \, year|i} = \frac{N}{T} \sum_{j=1}^{5} f_j \, E_{KM|i,j} \tag{12}$$

where i stands for the station index, N is the number of days in one year, T is the neap-spring tide time length, f_j is the frequency of occurrence associated with scenario Sj, and $E_{KM|i,j}$ is the available energy resource during the neap-spring tidal cycle for scenario Sj at station Pi.

The results presented in Table 6 show that the location with the highest potential for energy extraction is at station P8, with an
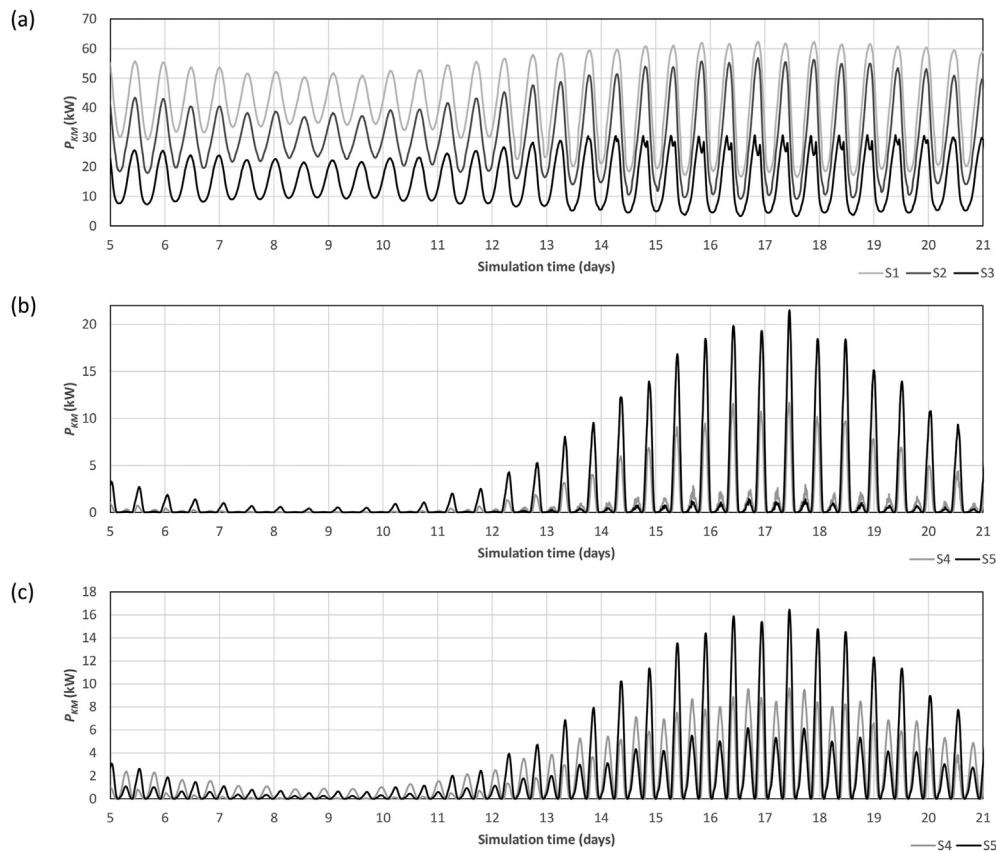
Fig. 7. Time evolution of the available power, P_{KM}. (a) at P8 for scenarios S1, S2 and S3, (b) at P0 for scenarios S4 and S5, (c) at P1 for scenarios S4 and S5. No cut-in velocity was considered.

estimated maximum annual available energy production of about 68 MW h. Nevertheless, it should be noticed that for this estimation, the entire depth was considered, and ideally, equipment should not exceed 85% of the depth at a particular location. Considering a turbine with $C_p = 0.40$ and a diameter $D = 0.85 h$, the annual available energy production for each selected station is presented in Table 7.

It should also be noticed that not all mechanic energy can be converted into electrical energy. This conversion depends on the efficiency of the transmission between the turbine and the generator and on the efficiency of the generator. Considering a global efficiency of 0.7 [49], the expected value for the produced energy is presented in Table 8. Knowing that the mean annual energy consumption per capita in Portugal in 2017 was 1200 kW h [36], this energy resource can complement but never fully replace other energy sources.

For those estuarine locations more influenced by the tide, as station P1, the annual available energy resource (3.4 MW h) can be compared with previous studies where the tide is the dominant factor for hydrokinetic exploitation. Alvarez et al. [17] obtained available energy resource values of 2.4 MW h at the Ria of Ribadeo (Galicia, Spain), and Pacheco et al. [26] and Fouz et al. [23] estimated an annual available energy resource of 5.7 MW h in the Faro channel (Ria Formosa, Portugal) and 2.26 MW h at the Minho estuary. Carballo et al. [14] obtained a maximum p_{KE} of 5 kW/m² associated with the tidal stream energy resource in the inner part of the Ria of Muros y Noya (Galicia, Spain) and Ramos and Iglesias [50] forecasted annual E_e values of 30.6 MW h for the Ria de Arosa (Galicia, Spain).

Tidal currents can be extremely efficient in certain locations,

even if no river flow is present. In this sense, the Galician and Portuguese Rias seem to be excellent locations for hydrokinetic energy resources exploitation because the tidal resource is amplified due to the geometry of the Rias. This is not the case of the Douro river estuary. In this estuarine region, high flow scenarios are the ones that produce more hydrokinetic energy, whereas tides are not strong enough to be considered for energy extraction. A turbine farm could be considered to increase the installed power and energy production, but too many turbines can choke the flow and reduce the available power [16]. Besides, and despite the comparatively low impact of this renewal energy production on ecosystems when compared to other energy sources, the installation of a hydrokinetic farm in the Douro estuary must be carefully analysed in terms of possible impacts on fauna and flora, as well as on navigation and human safety.

5. Conclusions

In estuarine regions, hydrokinetic energy can be obtained from a mixture of several forcings, being the most important the currents produced by tides and river flows. In order to define the areas with the greatest potential for the emplacement of new hydrokinetic energy farms, numerical models are required to properly analyse the combined influence of these drivers, simulating the hydrodynamic patterns, and quantifying the local kinetic power.

In this study, a shallow-water numerical model of estuarine hydrodynamics for the Douro estuary, previously calibrated and validated [35], was applied to examine the potential for exploitation of the estuarine hydrokinetic resource. Several scenarios were considered to represent the combined effects of the tides and river
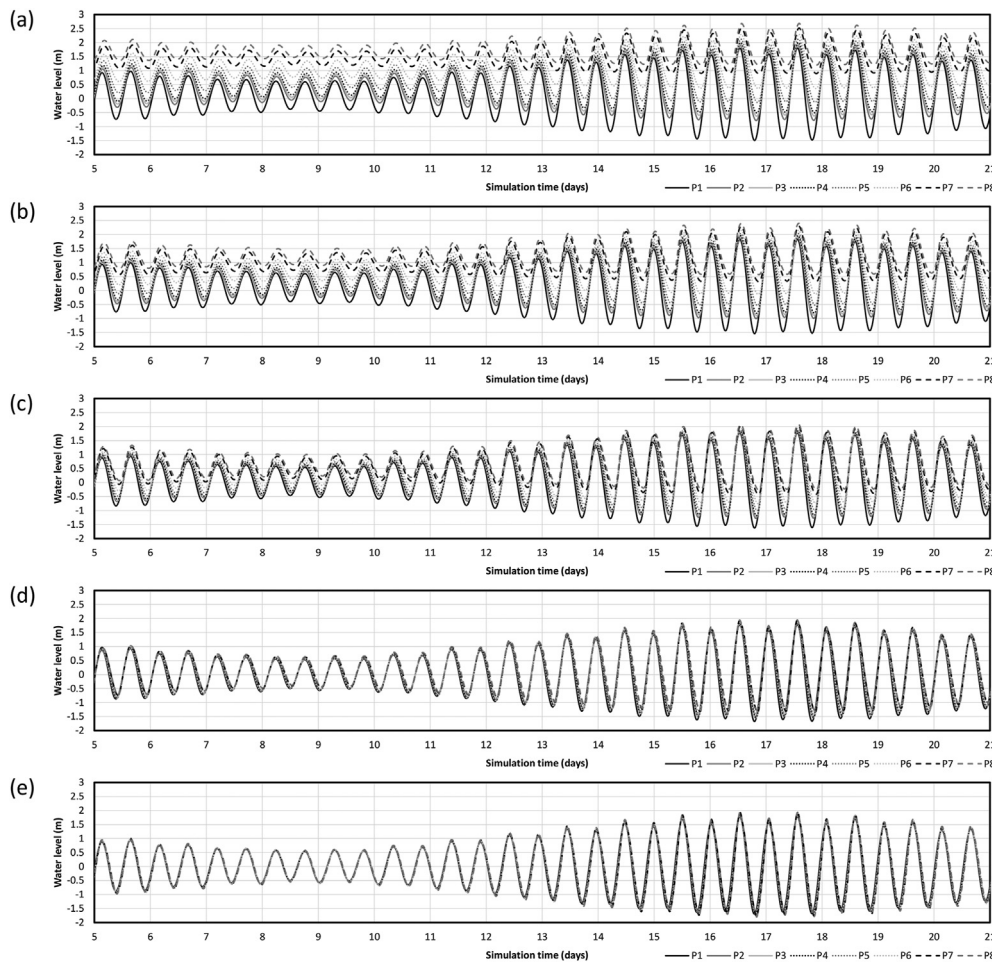
Fig. 8. Time series for the water elevation at stations P1−P8 for scenarios: (a) S1, (b) S2, (c) S3, (d) S4, and (e) S5.

Table 4
Tide surface elevation lag between stations P1 and P8.

Scenario	Lag (min)			
	Spring tide		Neap tide	
	High tide	Low tide	High tide	Low tide
S1	40	110	70	90
S2	30	100	60	80
S3	30	110	40	70
S4	0	80	20	50
S5	10	60	10	10

flow on hydrokinetic energy production.

This work demonstrates the importance of adequately selecting the estuarine locations for hydrokinetic energy extraction, based on the estuarine hydrodynamic configuration, as well as the utility of using parametric magnitudes not dependent on the characteristics of a specific equipment.

For the Douro estuary, the analysis of the water surface elevation and of the current velocity fields demonstrated a strong variability in the hydrodynamic behaviour that could affect the hydrokinetic energy production. The most promising region to install a hydrokinetic turbine is the upper part of the estuary, near the Crestuma-Lever dam, where the highest current velocities and the highest

available kinetic power were found. At this location, the maximum current velocity is achieved for mid-ebb tide conditions and strong river flows ($\sim$1500 m^3/s). Since even the largest river discharge imposed as a boundary condition was not strong enough to block the entrance of the tide into the estuarine region, it can be concluded that both drivers act together, always reinforcing the hydrokinetic energy production, during ebb tide. However, it is also shown that the tides in this estuary are not strong enough to induce a large hydrokinetic power on their own, and thus the main forcing for hydrokinetic energy production in this estuary is the river discharge.

In summary, the results obtained revealed that the Douro estuary presents some potential for the exploitation of hydrokinetic energy resources due to the currents produced by the river flow. However, the harvested energy will never be able to completely replace other energy resources. Future studies for this estuarine region must include more detailed numerical modelling experiments to assess the effect of hydrokinetic energy turbine or a turbine farm on the river flow, namely on the velocity fields and sedimentation processes, which may have some effects on the environment and on human activities (navigation, fishing, tourism, etc.). The security aspects of a turbine placement should also be carefully addressed. Since hydrokinetic turbines are still being further developed and their capacity is improving, a large array of devices and systems shall be considered to find the most adequate
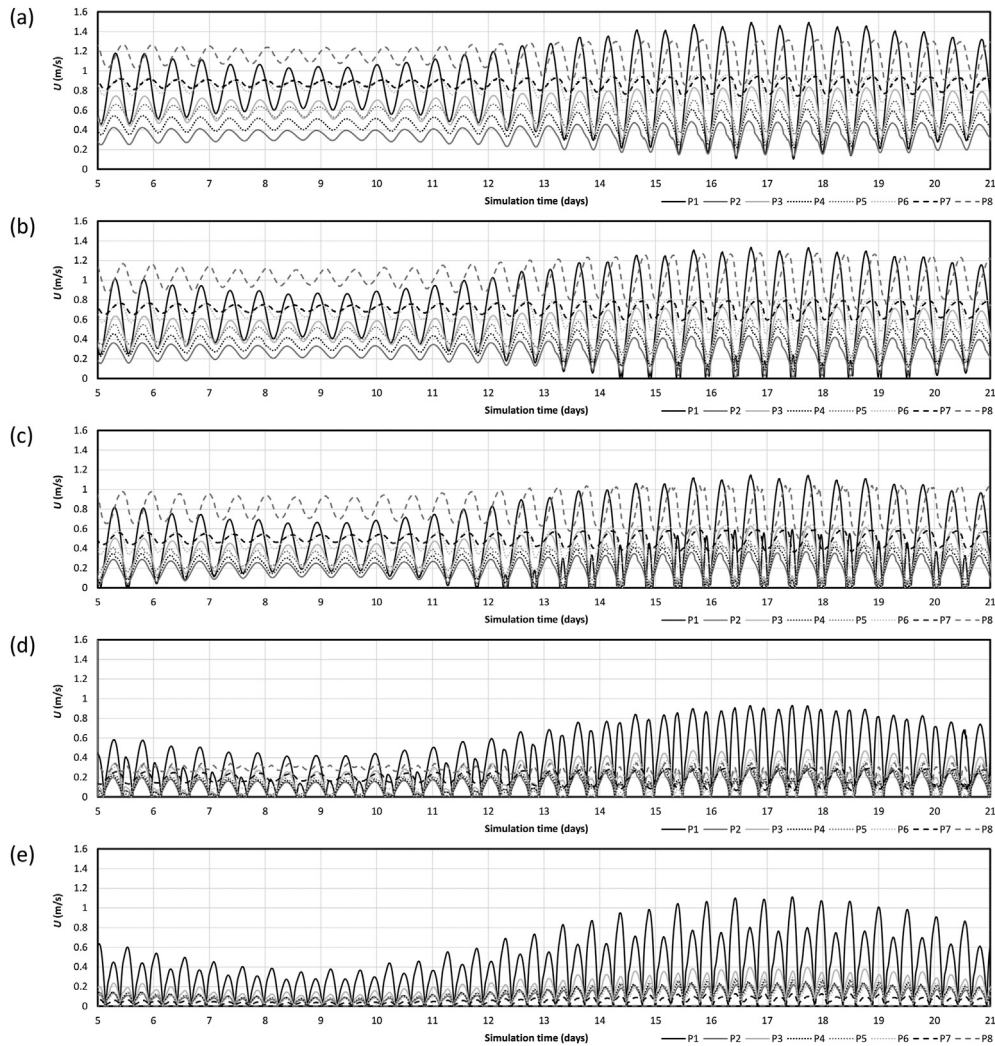
Fig. 9. Evolution of the current velocity at stations P1–P8 for scenarios: (a) S1, (b) S2, (c) S3, (d) S4, and (e) S5.

Table 5
Maximum available energy resource, E_{KM}, produced during a neap-spring tide cycle (15.4 days) for scenarios S1–S5 at stations P1–P8 considering a cut-in velocity $U_i = 0.7$ m/s.

E_{KM}	P1	P2	P3	P4	P5	P6	P7	P8
	(kW·h)	(kW·h)	(kW·h)	(kW·h)	(kW·h)	(kW·h)	(kW·h)	(kW·h)
S1-p95	3596	0	7756	0	36	8901	5016	15 173
S2-p90	2054	0	1464	0	0	3240	1861	11 031
S3-p80	883	0	0	0	0	0	0	4888
S4-p50	421	0	0	0	0	0	0	0
S5-p30	524	0	0	0	0	0	0	0

Table 6
Total available energy, $E_{KM\ year}$, during a year at stations P1–P8 considering a cut-in velocity $U_i = 0.7$ m/s.

$E_{KM\ year}$	P1	P2	P3	P4	P5	P6	P7	P8
(kW h)	21 159	0	15 987	0	62	21 051	11 924	68 028

Table 7
Total available energy, $E_{KM\ year}$, during a year at stations P1–P8 considering a cut-in velocity $U_i = 0.7$ m/s, a power coefficient $C_p = 0.4$, and a circular turbine with $D = 0.85\ h$.

$E_{KM\ year}$	P1	P2	P3	P4	P5	P6	P7	P8
(kW·h)	4803	0	3629	0	14	4778	2707	15 441

Table 8
Total available energy, $E_{KM\ year}$, during a year at stations P1–P8 considering a cut-in velocity $U_i = 0.7$ m/s, a power coefficient $C_p = 0.4$, a circular turbine with $D = 0.85\ h$ and an efficiency of 0.7.

$E_{KM\ year}$	P1	P2	P3	P4	P5	P6	P7	P8
(kW·h)	3362	0	2540	0	10	3345	1895	10 809

technology, in terms of configuration, size and energy production, for this estuarine region. The difference between the hydrokinetic power in nature and the total power that a device can harvest is large enough to expect that improved systems and optimum configuration could have the potential to help cover the increasing

energy needs of this region using renewable clean-energy sources.

Credit author statement

I. Iglesias: Conceptualization, Methodology, Software, Validation, Formal analysis, Investigation, Resources, Writing, Visualization. **A. Bio**: Software, Validation, Investigation, Resources, Investigation, Resources, Project administration, Funding acquisition. **L. Bastos**: Resources, Writing, Supervision, Project administration, Funding acquisition. **P. Avilez-Valente**: Methodology, Software, Validation, Formal analysis, Investigation, Resources, Writing, Visualization, Supervision.

Declaration of competing interest

The authors declare that they have no known competing financial interests or personal relationships that could have appeared to influence the work reported in this paper.

Acknowledgements

Notation

A	Swept area of the turbine
C_f	Dimensionless bottom friction coefficient
C_p	Power coefficient
D	Diameter of the turbine
d	Depth below the MSL
E_e	Available energy resource
E_{KM}	Maximum available energy resource
$E_{KM|i,j}$	Available energy resource for scenario Sj at station Pi
f	Coriolis parameter
f_j	Frequency of occurrence associated with scenario Sj
g	Acceleration due to gravity
H	Total water depth
h	Depth referred to the HZ
K_s	Strickler friction coefficient
N	Number of days in one year
p	Local pressure
p_E	Effective power density
p_{KE}	Power density
P_{KM}	Maximum available power
T	Time interval
U	Flow velocity
U_i	Cut-in velocity
U_o	Cut-off velocity
u	Vertically averaged velocity component in the x direction
v	Vertically averaged velocity component in the y direction
α	Energy coefficient
η	Free surface elevation above the MSL
η_{t-g}	Transmission−generator efficiency
ρ	Water density
ρ'	Anomaly density
ρ_0	Reference density
v_T	Eddy viscosity

References

[1] Iglesias I, Avilez-Valente P, Luís Pinho J, Bio A, Manuel Vieira J, Bastos L, et al. Numerical modeling tools applied to estuarine and coastal hydrodynamics: a user perspective. In: Antunes do carmo JS, editor. Coast. Mar. Environ. - phys. Process. Numer. Model., IntechOpen; 2019. p. 20. https://doi.org/10.5772/intechopen.85521.

[2] Dangendorf S, Wahl T, Hein H, Jensen J, Mai S, Mudersbach C. mean sea level variability and influence of the north atlantic oscillation on long-term trends in the German bight. Water 2012;4:170−95. https://doi.org/10.3390/w4010170.

[3] IPCC. Managing the risks of extreme events and disasters to advance climate change adaptation. Summary for policymakers. Cambridge, UK, and New York, NY, USA: Cambridge University Press; 2012.

[4] Ramos V, Carballo R, Álvarez M, Sánchez M, Iglesias G. A port towards energy self-sufficiency using tidal stream power. Energy 2014;71:432−44. https://doi.org/10.1016/j.energy.2014.04.098.

[5] Bahaj AS. Generating electricity from the oceans. Renew Sustain Energy Rev 2011;15:3399−416. https://doi.org/10.1016/j.rser.2011.04.032.

[6] Voss A. Waves, currents, tides-problems and prospects. Energy 1979;4(5): 823−31. https://doi.org/10.1016/0360-5442(79)90014-8.

[7] Güney MS, Kaygusuz K. Hydrokinetic energy conversion systems: a technology status review. Renew Sustain Energy Rev 2010;14:2996−3004. https://doi.org/10.1016/j.rser.2010.06.016.

[8] Johnstone CM, Nielsen K, Lewis T, Sarmento A, Lemonis G. EC FPVI co-ordinated action on ocean energy: a European platform for sharing technical information and research outcomes in wave and tidal energy systems. Renew Energy 2006;31(2):191−6. https://doi.org/10.1016/j.renene.2005.08.015.

[9] Ramos V, Carballo R, Sanchez M, Veigas M, Iglesias G. Tidal stream energy impacts on estuarine circulation. Energy Convers Manag 2014;80:137−49. https://doi.org/10.1016/j.enconman.2014.01.027.

[10] Petrie J, Diplas P, Gutierrez M, Nam S. Characterizing the mean flow field in rivers for resource and environmental impact assessments of hydrokinetic energy generation sites. Renew Energy 2014;69:393−401. https://doi.org/10.1016/j.renene.2014.03.064.

[11] Holanda P da S, Blanco CJC, Mesquita ALA, Brasil Junior ACP, de Figueiredo NM, Macêdo EN, et al. Assessment of hydrokinetic energy resources downstream of hydropower plants. Renew Energy 2017;101: 1203−14. https://doi.org/10.1016/j.renene.2016.10.011.

[12] Yuce MI, Muratoglu A. Hydrokinetic energy conversion systems: a technology status review. Renew Sustain Energy Rev 2015;43:72−82. https://doi.org/10.1016/j.rser.2014.10.037.

[13] Myers LE, Bahaj AS. An experimental investigation simulating flow effects in first generation marine current energy converter arrays. Renew Energy 2012;37(1):28−36. https://doi.org/10.1016/j.renene.2011.03.043.

[14] Carballo R, Iglesias G, Castro A. Numerical model evaluation of tidal stream energy resources in the Ría de Muros (NW Spain). Renew Energy 2009;34: 1517−24. https://doi.org/10.1016/j.renene.2008.10.028.

[15] Bahaj AS, Myers LE. Fundamentals applicable to the utilisation of marine current turbines for energy production. Renew Energy 2003;28(14):2205−11. https://doi.org/10.1016/S0960-1481(03)00103-4.

[16] Brooks DA. The hydrokinetic power resource in a tidal estuary: the Kennebec River of the central Maine coast. Renew Energy 2011;36:1492−501. https://doi.org/10.1016/j.renene.2010.10.029.

[17] Álvarez M, Ramos V, Carballo R, Arean N, Torres M, Iglesias G. The influence of dredging for locating a tidal stream energy farm. Renew Energy 2020;146: 242−53. https://doi.org/10.1016/j.renene.2019.06.125.

[18] González-Caballín JM, Álvarez E, Guttiérrez-Trashorras AJ, Navarro-Manso A, Fernández J, Blanco E. Tidal current energy potential assessment by a two dimensional computational fluid dynamics model: the case of Avilés port (Spain). Energy Convers Manag 2016;119:239−45. https://doi.org/10.1016/j.enconman.2016.04.060.

[19] Ahmadian R, Falconer RA. Assessment of array shape of tidal stream turbines on hydro-environmental impacts and power output. Renew Energy 2012;44: 318−27. https://doi.org/10.1016/j.renene.2012.01.106.

[20] Shapiro GI. Effect of tidal stream power generation on the region-wide circulation in a shallow sea. Ocean Sci 2011;7:165−74. https://doi.org/10.5194/os-7-165-2011.

[21] Neill SP, Litt EJ, Couch SJ, Davies AG. The impact of tidal stream turbines on large-scale sediment dynamics. Renew Energy 2009;34(12):2803−12. https://

doi.org/10.1016/j.renene.2009.06.015.

[22] Kadiri M, Ahmadian R, Bockelmann-Evans B, Rauen W, Falconer R. A review of the potential water quality impacts of tidal renewable energy systems. Renew Sustain Energy Rev 2012;16(1):329–41. https://doi.org/10.1016/j.rser.2011.07.160.

[23] Fouz DM, Carballo R, Ramos V, Iglesias G. Hydrokinetic energy exploitation under combined river and tidal flow. Renew Energy 2019;143:558–68. https://doi.org/10.1016/j.renene.2019.05.035.

[24] Iglesias I, Avilez-Valente P, Bio A, Bastos L. Modelling the main hydrodynamic patterns in shallow water estuaries: the Minho case study, vol. 11. Switzerland: Water; 2019. https://doi.org/10.3390/w11051040.

[25] Bastos L, Bio A, Iglesias I. The importance of marine observatories and of RAIA in particular. Front Mar Sci 2016;3:1–11. https://doi.org/10.3389/fmars.2016.00140.

[26] Pacheco A, Ferreira Ó, Carballo R, Iglesias G. Evaluation of the production of tidal stream energy in an inlet channel by coupling field data and numerical modelling. Energy 2014;71:104–17. https://doi.org/10.1016/j.energy.2014.04.075.

[27] Gómez-Gesteira M, Gimeno L, DeCastro M, Lorenzo MN, Alvarez I, Nieto R, et al. The state of climate in NW Iberia. Clim Res 2011;48:109–44. https://doi.org/10.3354/cr00967.

[28] Bastos L, Bio A, Pinho JLS, Granja H, Jorge da Silva A. Dynamics of the Douro estuary sand spit before and after breakwater construction. Estuar Coast Shelf Sci 2012;109:53–69. https://doi.org/10.1016/j.ecss.2012.05.017.

[29] Portela LI. Sediment transport and morphodynamics of the Douro River estuary. Geo Mar Lett 2008;28:77–86. https://doi.org/10.1007/s00367-007-0091-1.

[30] Azevedo IC, Bordalo AA, Duarte PM. Influence of river discharge patterns on the hydrodynamics and potential contaminant dispersion in the Douro estuary (Portugal). Water Res 2010;44:3133–46. https://doi.org/10.1016/j.watres.2010.03.011.

[31] Pinto J, Silva AJ, Hidrográfico I, Trinas R. Tide propagation in the Douro river estuary. Portugal); 2007. p. 49.

[32] Reis J. Caracterização da Maré do Porto de Leixões. 2005.

[33] Iglesias I, Almeida CMR, Teixeira C, Mucha AP, Magalhães A, Bio A, et al. Linking contaminant distribution to hydrodynamic patterns in an urban estuary: the Douro estuary test case. Sci Total Environ 2020;707:135792. https://doi.org/10.1016/j.scitotenv.2019.135792.

[34] Granja H, Bastos L, Pinho J, Gonçalves J, Henriques R, Bio A, et al. Integração de metodologias no estabelecimento de um programa de monitorização costeira para avaliação de risco. VII Conferência Nac. Cartogr. e Geod.; 2011. p. 11.

[35] Iglesias I, Venâncio S, Pinho JL, Avilez-Valente P, Vieira JMP. Two models solutions for the Douro estuary: flood risk assessment and breakwater effects. Estuar Coast 2019;42:348–64. https://doi.org/10.1007/s12237-018-0477-5.

[36] Pordata. Base de Dados sobre Portugal contemporâneo. 2019. https://www.pordata.pt/. [Accessed 11 April 2019].

[37] IH - Instituto Hidrográfico. http://www.hidrografico.pt/; 2019.

[38] Hervouet JM. Hydrodynamics of free surface flows: modelling with the finite element method. 2007. https://doi.org/10.1002/9780470319628.

[39] Lynch DR, Gray WG. A wave equation model for finite element tidal computations. Comput Fluids 1979;7(3):207–28. https://doi.org/10.1016/0045-7930(79)90037-9.

[40] Becker JJ, Sandwell DT, Smith WHF, Braud J, Binder B, Depner J, et al. Global bathymetry and elevation data at 30 arc seconds resolution: SRTM30_PLUS. Mar Geod; 2009. https://doi.org/10.1080/01490410903297766.

[41] Krige DG. A statistical approach to some mine valuations and allied problems at the witwatersrand. University of Witwatersrand; 1951.

[42] Matheron G. Principles of geostatistics. Econ Geol 1963;58(8):1246–66. https://doi.org/10.2113/gsecongeo.58.8.1246.

[43] Egbert GD, Bennett AF, Foreman MGG. TOPEX/POSEIDON tides estimated using a global inverse model. J Geophys Res 1994;99(C12):24821–52. https://doi.org/10.1029/94JC01894.

[44] Azevedo IC, Duarte PM, Bordalo AA. Pelagic metabolism of the Douro estuary (Portugal) - factors controlling primary production. Estuar Coast Shelf Sci 2006;69:133–46. https://doi.org/10.1016/j.ecss.2006.04.002.

[45] deCastro M, Gómez-Gesteira M, Lorenzo MN, Alvarez I, Crespo AJC. Influence of atmospheric modes on coastal upwelling along the western coast of the Iberian Peninsula, 1985 to 2005. Clim Res 2008;36:169–79. https://doi.org/10.3354/cr00742.

[46] Pinto J. Influência do Regime de Escoamento Fluvial na Hidrologia e Dinâmica do Estuário do Douro. Universidade de Évora.; 2007.

[47] Chow VT. Open-channel hydraulics. New York: Ven Te Chow. McGraw-Hill; 1959. xviii + 680 pp. Illus. $17. 1959.

[48] Murray R, MacIver R, Reddy N, Venugopal V, Baston S, Waldman S, et al. TeraWatt position papers: a "toolbox" of methods to better understand and assess the effects of tidal and wave energy arrays on the marine environment. 2015.

[49] Münch-Alligné C, Schmid J, Richard S, Gaspoz A, Brunner N, Hasmatuchi V. Experimental assessment of a new kinetic turbine performance for artificial channels, vol. 10. Switzerland: Water; 2018. https://doi.org/10.3390/w10030311.

[50] Ramos V, Iglesias G. Performance assessment of tidal stream turbines: a parametric approach. Energy Convers Manag 2013;69:49–57. https://doi.org/10.1016/j.enconman.2013.01.008.

[51] Oceanflow energy. 2020. http://www.oceanflowenergy.com/.

[52] Hu Z, Du X. Reliability analysis for hydrokinetic turbine blades. Renew Energy 2012;48:251–62. https://doi.org/10.1016/j.renene.2012.05.002.

[53] Chen CT, Bradshaw A, Schleicher K. A new high pressure equation of state for seawater. Deep Sea Res Part A, Oceanogr Res Pap 1980;27(3–4):255–64. https://doi.org/10.1016/0198-0149(80)90016-3.